ACS APPLIED ENERGY MATERIALS

www.acsaem.org Article

Probing the Evolution of Active Sites in MoO_2 for Hydrogen Generation in Acidic Medium

Chandraraj Alex, Rajkumar Jana, Vivek Ramakrishnan, Muhammed Safeer Naduvil Kovilakath, Ayan Datta, Neena S. John,* and Akhil Tayal

Cite This: *ACS Appl. Energy Mater.* 2023, 6, 5342−5351 Read Online

ACCESS | Metrics & More | Article Recommendations | Supporting Information

ABSTRACT: MoO_2 is an effective host and catalytic material for electrochemical hydrogen evolution reaction in the form of composites, heterostructures, core−shell structures, and doped systems. Using pristine MoO_2 as the electrocatalyst is less known due to a lack of knowledge of the active sites and their development during the hydrogen evolution reaction (HER). In this work, we have correlated the active-site evolution on applying a cathodic potential to pristine MoO_2 and the corresponding improvement in catalytic activity. The activity enhancement is observed as a progressive reduction of overpotential from 0.62 to 0.42 V (vs RHE) at 1 mA/cm^2 during potential cycles accompanied by a tremendous lowering of the Tafel slope (b) from 127 to 72 mV/dec. The decreased b value reveals that the developed active sites hasten the reaction via a change in the rate-determining step from Volmer to Heyrovsky. The changes in the Mo oxidation states and the local coordination environment of Mo−O are monitored by advanced X-ray absorption spectroscopy, unfolding the emergence of active sites in MoO_2 through a change of Mo−O coordination from octahedral (O_h) to the coordinatively unsaturated distorted O_h environment with a lowering of the Mo−O coordination number and oxidation states of Mo ions. The key thermodynamic and kinetic parameters, namely, the change in Gibbs free energy for hydrogen adsorption on the catalyst surface and the kinetic activation barrier related to the HER rate-determining step for both activated (MoO_{2-x}) and pristine MoO_2, have been simulated and rationalized with the experimental results.

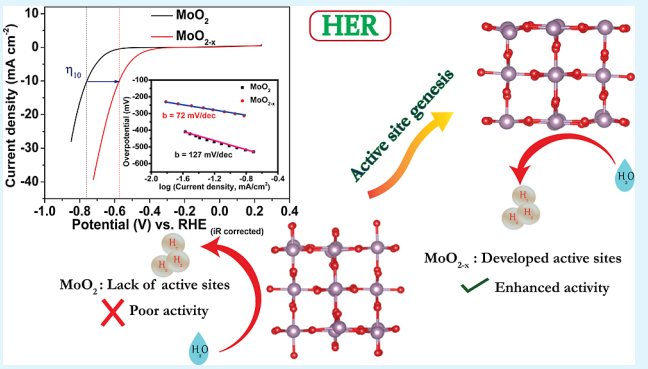

KEYWORDS: *electrochemical cycling, active sites, O_h distortion, Mo−O local environment, Mo oxidation state, HER kinetics*

INTRODUCTION

Electrochemical water splitting is an emerging technology for renewable hydrogen production.[1,2] Water electrolysis consists of two half-cell reactions: hydrogen and oxygen evolution.[3] Many non-noble-metal-based electrocatalysts are reported for the electrochemical hydrogen evolution reaction (HER).[4−6] Among them, metal oxides are considered to be more accessible with respect to various aspects of synthesis, availability, and flexibility.[7] They are amenable to property tuning by varying the metal to oxygen ratios or facile coupling with other active systems through heterostructure formation and core−shell structures such as oxide/sulfide, oxide/carbide, oxide/nitride systems, etc.[8−10] Generally, metal oxide-based HER catalysts have poor activity as their hydrogen adsorption free energy is far away from zero ($\Delta G_{H^*} \neq 0$).[11,12] Hence, strategies involving doping, defect engineering, and coupling with other active HER materials are adopted to improve the activity.[6,13−21] In the case of pristine MoO_3 and MoO_2, the intrinsic weak electrocatalytic HER activity can be drastically improved through oxygen-deficient defect engineering. It has been shown that mesoporous MoO_{3-x} and α-MoO_3 can be enabled for HER catalysis by introducing Mo^{5+} ions or oxygen vacancies.[22,23] On the other hand, MoO_2 is an excellent conductive material.[24,25] However, the as-synthesized, pristine MoO_2 exhibits poor HER activity due to a lack of active sites and is often post-treated or combined with other active materials to enhance HER activity.[26−30] Hence, generation of active sites in the pristine MoO_2 system is of great significance for its future usage as a catalyst for hydrogen production. Wang et al. introduced oxygen vacancies in MoO_2 (grown on Ni foam) through the hydrazine reduction method, and activity enhancement was observed.[31] Nanoflower-like MoO_2 has been synthesized on nickel foam, followed by post-synthesis annealing in hydrogen that showed excellent activity close to that of Pt in an alkaline medium. The authors explain that

Received: February 5, 2023
Accepted: April 17, 2023
Published: May 2, 2023

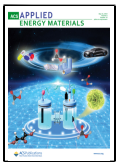

https://doi.org/10.1021/acsaem.3c00320
ACS Appl. Energy Mater. 2023, 6, 5342−5351

porous morphology, high surface area with good electrical conductivity, and enhanced Mo^{4+} ions after hydrogen treatment are the reasons for efficient HER.[26] In our previous study of MoO_2 films grown on fluorine-doped tin oxide by the hydrothermal method, we have shown that annealing in hydrogen significantly improves the HER activity and observed a change in MoO_2 crystallite plane orientation upon hydrogen annealing.[27] In the case of Ni-incorporated MoO_2, the enhanced HER activity and stability obtained in an alkaline medium are explained due to the presence of Ni influencing the surface charge concentration and shift in the active sites from Mo to O at the interface with upraising of the O 2p orbital in MoO_2, thereby strengthening hydrogen adsorption.[28] In another report, Ni doping in the MoO_2 lattice is seen to modulate the electron density at MoO_2 by causing electron deficiency in neighboring O sites, and this catalyst exhibits high HER and HOR activity in acidic electrolytes.[29] Hierarchically structured 1D MoO_2 synthesized in ionic liquid is reported to exhibit excellent HER activity in acidic medium. The superior activity is explained due to the high surface area, many active sites at kinks and edges, and good charge transport.[30] In the case of highly dispersed MoO_2 in nitrogen-doped porous carbon nanosheets supported on Ni foam, the authors explain that the better HER activity in alkaline media is caused by abundant pores, superior electrical conductivity, specific surface area, and synergic effect between N-doped carbon and MoO_2.[32]

In most cases of pristine MoO_2, synthesized by various routes or those subjected to post-synthesis treatment, there is a lack of understanding of the formation of active sites or defects responsible for improving HER activity. In a recent theoretical paper, S−H Lin and Kuo addressed the tuning of defects in MoX_2 for achieving free energy of hydrogen adsorption close to zero. For MoO_2, the variation of the x atom in defective MoO_{2-x} from 0.0625 to 0.25 helps to attain optimum hydrogen adsorption energy and enhanced HER activity[33] but requires experimental support. There is a need to comprehend the identification of such active- or defective-site development and the local environment of Mo in the active state of catalysts for designing efficient catalysts for sustainable hydrogen production.

In order to investigate the active or oxygen-deficient defective site formation, we have subjected MoO_2 films on fluorine-doped tin oxide (FTO) substrates to potential cycling. The as-synthesized MoO_2 shows poor HER activity, while it gets improved with electrochemical cycling in an acidic medium. The activity enhancement is analyzed through overpotential, Tafel slope, and impedance study. In this manuscript, we present a systematic investigation of the surface composition, local geometry, and oxidation state of Mo in pristine and electrochemically activated MoO_2 by X-ray absorption spectroscopy and X-ray photoelectron spectroscopy to unfold the active-site formation. A reduction of Mo-ion oxidation states generating MoO_{2-x} as the active material after electrochemical activation, along with a change in the local coordination of MoO_2 from octahedral (O_h) to coordinatively unsaturated distorted O_h during HER and a lowering of Mo−O coordination number, is revealed. Additionally, a theoretical study is presented revealing that the formed sites in the in-situ-generated MoO_{2-x} surface can drastically lower the hydrogen adsorption free energy, ΔG_{H^*} close to zero, with Heyrovsky as a rate-determining step for enhanced electrochemical hydrogen production. The study aims to provide a better understanding of the active sites of pristine MoO_2 in imparting better HER activity.

MATERIALS AND METHODS

Materials. Anhydrous citric acid ($C_6H_8O_7$, purity 99.5%) is purchased from Spectrochem. Pvt. Ltd. Ammonium heptamolybdate tetrahydrate ($(NH_4)_6Mo_7O_{24}\cdot 4H_2O$, purity ≥ 99%) is purchased from Merck. Fluorine-doped tin oxide (FTO)-coated glass (SnO_2/F, resistivity < 7 Ω/sq) is purchased from Shilpa Enterprises, India. 65% of nitric acid is purchased from Merck. 0.5 M H_2SO_4 solution (pH 0) is prepared from 98% (Merck) concentrated sulfuric acid, and all electrolyte solutions are prepared from ultrapure (type-1) water.

Synthesis of MoO_2. The synthesis route earlier reported from our laboratory was adopted.[27] The FTO substrates (area of 1 × 2 cm^2) were washed with a 1:1 volume ratio of HNO_3 and H_2SO_4 solution followed by ultrapure water and isopropyl alcohol (IPA). 1.2 g of $(NH_4)_6Mo_7O_{24}\cdot 4H_2O$ and 1 g of citric acid were dissolved in 40 mL of ultrapure water, transferred into a Teflon-lined autoclave containing an inclined FTO (the conductive surface facing downward), and heated in an oven for 16 h at 200 °C. After the reaction, the autoclave is cooled at ambient temperature, and FTO samples are taken out and washed many times with ultrapure water. FTO surfaces are seen to be coated with a brownish black MoO_2 film. The film is annealed in vacuum (pressure 10^{-3} bar) at 500 °C for 2 h.

Material Characterization. The crystal structures of films on FTO are probed by a Rigaku Smart Lab X-ray diffractometer equipped with parallel beam optics, and X-ray diffraction (XRD) patterns are acquired with Cu Kα radiation incident at a glancing angle of 0.3°. Raman spectroscopy was used for chemical nature analysis with an excitation wavelength of 532 nm (Horiba Jobin Yvon XploRA PLUS V1.2 MULTILINE). The chemical nature of the samples was examined through a Kratos X-ray photoelectron spectrometer—AXIS Ultra spectrometer integrated with a charge neutralization system, magnetic immersion lens, and spherical mirror analyzer. The monochromatic Al Kα X-rays with an energy of 1486.6 eV were focused on the samples to obtain the high-resolution spectra. The morphology of the catalyst and crystal structure are monitored using field emission scanning electron microscopy (FESEM, Tescan-Mira 3 LMH) and transmission electron microscopy (TEM, TALOS F200S G2 at 200 kV acceleration voltage). All X-ray absorption spectroscopy (XAS) measurements were carried out ex-situ at Deutsches Elektronen-Synchrotron (DESY), Petra III P64 beamline at Hamburg.[34] Mo K-edge XAS was measured using a Si(111) monochromator and a passivated implanted planar silicon detector (PIPS) in the fluorescence mode. Multiple scans were accumulated and later merged to improve the signal-to-noise ratio. The X-ray absorption fine structure (XAFS) data were processed using Demeter software package following the standard background subtraction procedure through Athena software.[35] Further fitting details and fitted data are given in the Supporting Information.

Electrochemical Characterization. The electrochemical studies were carried out using a CHI760E instrument with a three electrode setup. Hydrothermally grown MoO_2 films on FTO, coated with 10 μL of Nafion (1 wt %), were used as the working electrode; graphite rod and $Hg/HgSO_{4(sat.\ K_2SO_4)}$ were used as the counter and reference electrodes, respectively. The electrolyte used was 0.5 M H_2SO_4 at pH 0. Linear sweep voltammetry (LSV) studies were carried out at a scan rate of 5 mV/s, and electrochemical activation was performed at a scan rate of 100 mV/s. The cyclic voltammograms (CV) were carried out at different scan rates in the potential window of −0.34 to −0.44 V vs $Hg/HgSO_{4(sat.\ K_2SO_4)}$ to calculate the electrochemical surface area (ECSA) of catalysts before and after activation. Impedance spectra were acquired in the 10^{-2} to 10^6 Hz frequency range.

Computational Details. All the spin-polarized calculations were performed within the framework of density functional theory (DFT) using the plane-wave technique as implemented in the Vienna Ab initio Simulation Package (VASP).[36] The generalized gradient approximation method (GGA) parameterized by the Perdew−Burke−Ernzerhof (PBE) was used to account for the exchange−

https://doi.org/10.1021/acsaem.3c00320
ACS Appl. Energy Mater. 2023, 6, 5342−5351

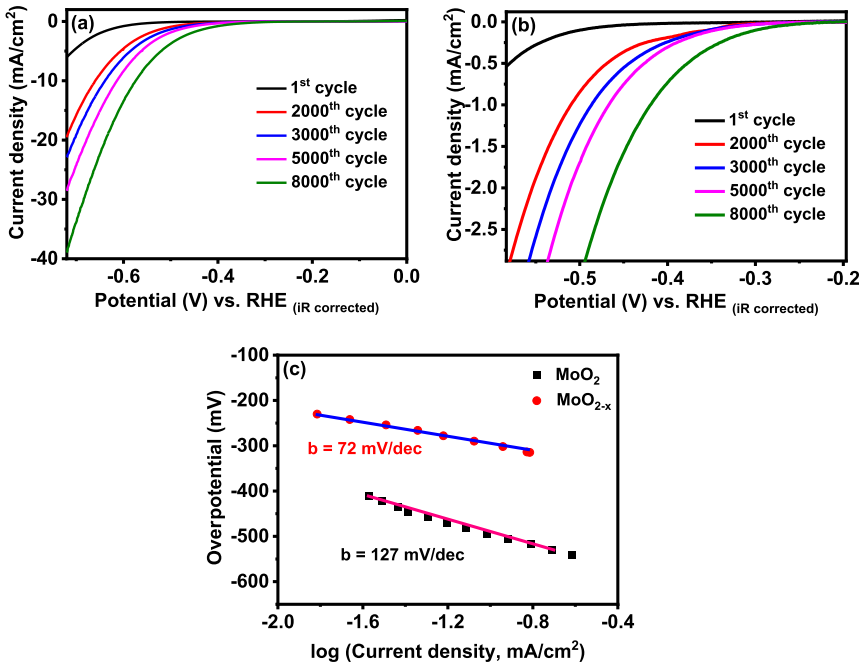

Figure 1. (a) LSV of MoO_2 films on FTO during various potential cycling in 0.5 M H_2SO_4 electrolyte with graphite as the counter electrode, (b) expanded LSV curves of (a) in the desired potential region, and (c) Tafel plots of MoO_2 before and after electrochemical activation (MoO_{2-x}).

correlation energy.[37] The DFT + U method was used to account for the on-site coulomb repulsion and improve the description of localized Mo d-electrons in Mo oxides with U_{eff} = −1.0 eV as recommended by the previous studies.[38] We used the projector augmented wave potential (PAW) to treat the ion−electron interactions. For describing the effect of van der Waals interactions, the DFT-D2 empirical correction method proposed by Grimme was applied.[39] In all computations, the kinetic energy cutoff is set to be 500 eV in the plane-wave expansion. All the structures were fully relaxed (both lattice constant and atomic position) using the conjugated gradient method. The convergence threshold was set to be 10^{-4} eV in energy and 0.01 eV/Å in force. For geometry optimization, the Brillouin zone was sampled using a 5 × 5 × 1 Monkhorst−Pack k-point mesh, while a higher 7 × 7 × 1 Monkhorst−Pack grid was used to calculate the electronic density of states (DOS). The climbing image nudged elastic band method (CI-NEB) was used to calculate the energy activation barriers for different HER pathways. Six intermediate images were considered along the minimum energy pathway (MEP) to search for a transition state. The activation barriers were calculated for all the pathways using the following equations: $\Delta E^{\ddagger} = E_{TS} - E_{IS}$ and $\Delta E = E_{FS} - E_{IS}$, where IS, TS, and FS correspond to the initial, transition, and final state, respectively.

The relative free energy of adsorbed atomic hydrogen (H*) was calculated as[40,41]

$$\Delta G_{H^*} = \Delta E_{H^*} + 0.20 \quad (1)$$

where ΔE_{H^*} (i.e., H* adsorption energy) on different MoO_2 surfaces were determined using the relation

$$\Delta E_{H^*} = E_{surface+H^*} - E_{surface} - 1/2E_{H^2} \quad (2)$$

where $E_{surface}$ and $E_{surface}$ + H* are total energies of the pristine and H* adsorbed surfaces, respectively, while E_{H_2} is the energy of H_2 in the gas phase.

In order to model (110) surface of MoO_2, we considered a five-layered periodic rectangular slab of the cell (5.73 × 7.47 Å^2) with 48 atoms (16 Mo and 32 O atoms are used, 1:2 ratio), while the defected MoO_2 (110) (i.e., MoO_{2-x} (110)) surface was modeled with a rectangular five-layered periodic slab of the surface cell (5.56 × 7.44 Å^2) with 42 atoms (16 Mo and 26 O atoms are used, 1:1.63 ratio). A vacuum layer of 20 Å was used in the direction perpendicular to the surfaces (along the *Z*-direction) to avoid spurious interactions between the neighboring slabs. The nearest distance between the two adsorbed hydrogen atoms in the adjacent supercell is ∼6 Å.

RESULTS AND DISCUSSION

The MoO_2 film on FTO obtained by hydrothermal synthesis is subjected to potential cycles under electrochemical conditions in the applied potential range of 0 to −0.66 V vs $RHE_{(iR\ corrected)}$. Interestingly, the HER activity improves significantly with an increasing number of potential cycles in the acidic medium in terms of the increased current density and lowering of overpotential (Figure 1a,b). The surface of the as-synthesized MoO_2 can be considered to become activated during the potential cycling process. The linear sweep voltammetry (LSV) of the as-synthesized MoO_2 film on FTO in 0.5 M H_2SO_4 electrolyte (pH 0) gives a current density of 1 mA/cm^2 at an applied potential of −0.61 V, and it gradually reduces to −0.50 V after 2000 cycles (Figure 1a,b). Furthermore, the overpotential at a current density of 1 mA/cm^2 gradually reduces to −0.48, −0.46, and −0.42 V, corresponding to 3000, 5000, and 8000 activation cycles, respectively. The 8000 cycles of activated MoO_2 are denoted as MoO_{2-x}. The oxygen-deficient defects in MoO_2 might arise through the following electrochemical reduction reactions i and ii

$$MoO_2 + x{\cdot}H^+ + x{\cdot}e^- \rightarrow MoO_{2-x}(OH)_x \quad (i)$$

$$MoO_{2-x}(OH)_x + x{\cdot}H^+ + x{\cdot}e^- \rightarrow MoO_{2-x} + x{\cdot}H_2O \quad (ii)$$

The above in situ electrochemical reduction reaction is assisted by the hydrogen evolution reaction. The above type of reduction mechanism has been reported for the chemical reduction of MoO_3 into MoO_2 during hydrogen annealing.[42] The LSV curves without iR corrections are given in Figure S1a. The activation could be effectively monitored only until 8000

https://doi.org/10.1021/acsaem.3c00320
ACS Appl. Energy Mater. 2023, 6, 5342−5351

cycles due to the gradual peel-off of the MoO_2 film from FTO caused by electrochemical reaction conditions such as highly acidic pH and prolonged electrolyte exposure with an increasing number of potential cycles. Hence, we see a slight increase in overpotential for the 10,000 potential cycles, from −0.42 (8000 cycles) to −0.44 V (10,000 cycles), at a current density of 1 mA/cm^2 due to the film instability (Figure S1b). The LSV for bare FTO under similar potential cycling conditions indicates degradation of FTO and is given in Figure S2.

Overall, the HER potential gets lowered by 0.2 V at 1 mA/cm^2 during electrochemical activation of MoO_2 (8000 cycles of activation) (Figure 1b). The Tafel slope also shows a drastic decrease from 127 mV/dec for the as-synthesized MoO_2 to 72 mV/dec for electrochemically activated MoO_{2-x} (Figure 1c). The lowering of Tafel slope indicates faster kinetics for HER on the activated surface with a probable change in the rate-determining step, which will be discussed later in this section.

The activation process of pristine MoO_2 during electrochemical cycling offers an ideal system for probing the evolution of active sites without the influence of any dopants. Any insights concerning the active sites of MoO_2 could be revealed by characterizing MoO_2 itself before and after activation. Hence, we have utilized the electrochemical activation process to understand the active-site formation in MoO_2 with detailed morphological, structural, and chemical environment analysis of the pristine and activated systems.

A comparison of the XRD patterns of the pristine MoO_2 with that of activated MoO_{2-x} is presented in Figure 2. The

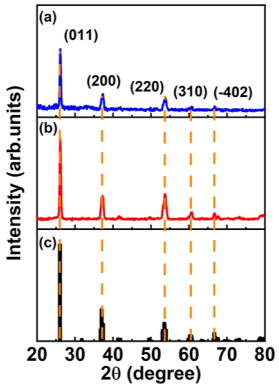

Figure 2. XRD patterns of (a) activated MoO_{2-x} and (b) pristine MoO_2 and (c) simulated XRD pattern of monoclinic MoO_2.

pristine MoO_2 shows diffraction peaks at 26.10, 37.25, 53.69, 60.80, and 66.71° that correspond to (011), (200), (220), (310), and (−402) planes of monoclinic MoO_2, respectively (JCPDS no. 65-1273) (Figure 2b).[43] The pattern does not show any significant changes after electrochemical activation (Figure 2a), indicating that the active state of the catalyst does not undergo any bulk changes in its crystal structure during cycling and HER. The FTO peaks are not observed in XRD and might be due to the thick MoO_2 film on FTO and data acquisition being performed in the grazing incidence mode.

The transmission electron microscopy (TEM) images exhibit disc-like crystallites for MoO_2 with a d spacing of 0.34 nm corresponding to the (011) plane of monoclinic MoO_2 (Figure 3a,b). The electrochemical activation does not seem to alter the morphology of MoO_2 (Figure 3c) or the crystallite structure (Figure 3d). The selected area electron

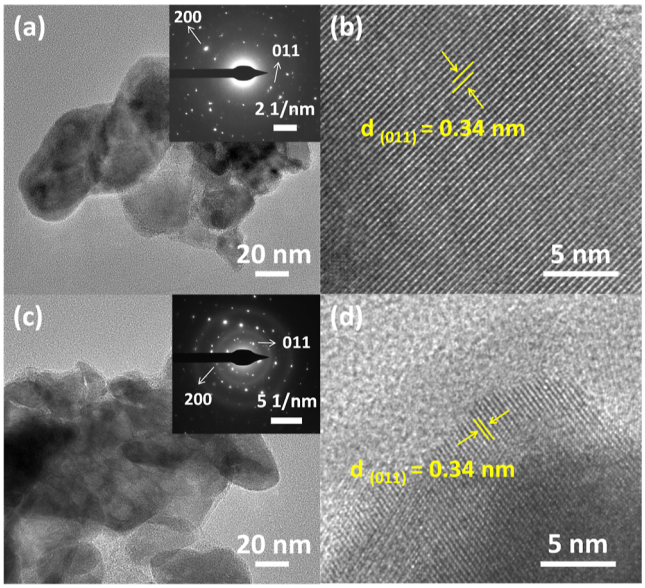

Figure 3. (a,b) TEM and HRTEM images of pristine MoO_2. (c,d) TEM and HRTEM images of activated MoO_{2-x}. Insets show corresponding SAED patterns.

diffraction (SAED) patterns of MoO_2 before and after electrochemical activation are given in the insets of Figure 3a,c. The observed diffraction spots belong to (011) and (200) planes of monoclinic MoO_2. Field emission scanning electron microscopy (FESEM) images of the as-synthesized, pristine MoO_2 film on FTO and the catalyst surface after electrochemical cycling also show similar crystallite morphology (Figure S3).

The chemical changes of MoO_2 and its activated state, MoO_{2-x}, are analyzed by Raman spectroscopy. The Raman spectra show peaks at 197, 222, 348, 486, 564, and 727 cm^{-1} for the as-synthesized MoO_2 (Figure 4). The Raman peaks at

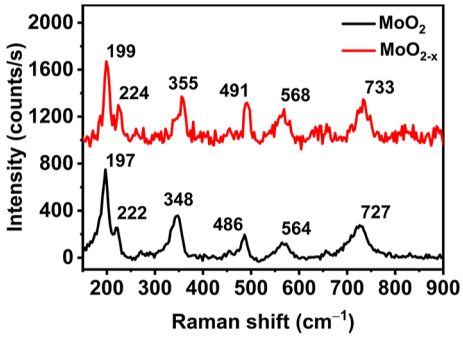

Figure 4. Raman spectra of the as-synthesized and electrochemically activated MoO_2.

727 and 564 cm^{-1} belong to stretching vibrations of Mo−O(I) and Mo−O(II) groups in the MoO_2 lattice.[44] The other peaks at 486, 348, 222, and 197 cm^{-1} are attributed to the phonon vibration modes of MoO_2.[27,45] The electrochemically activated MoO_{2-x} gives the blue-shifted peaks at 199, 224, 355, 491, 568, and 733 cm^{-1}. Camacho-López et al. studied the Raman spectra of MoO_x transformation from monoclinic MoO_2 to α-MoO_3 through laser irradiation and reported a red shift in the Raman spectra of the formed intermediate before conversion into the oxidized state of α-MoO_3.[46] The blue shift observed

https://doi.org/10.1021/acsaem.3c00320
ACS Appl. Energy Mater. 2023, 6, 5342−5351

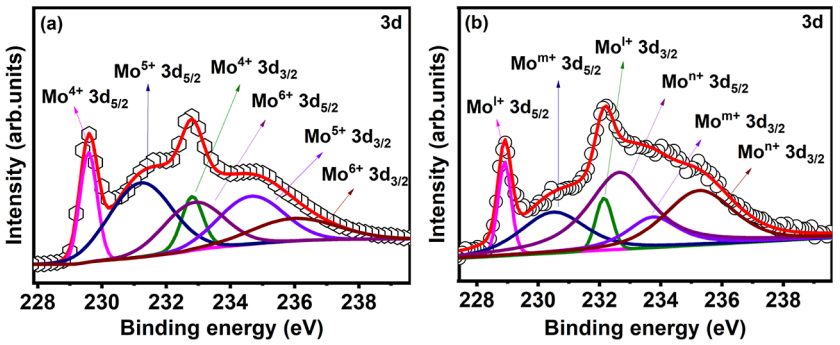

Figure 5. X-ray photoelectron spectra of Mo 3d (a) pristine MoO_2 and (b) activated MoO_{2-x}.

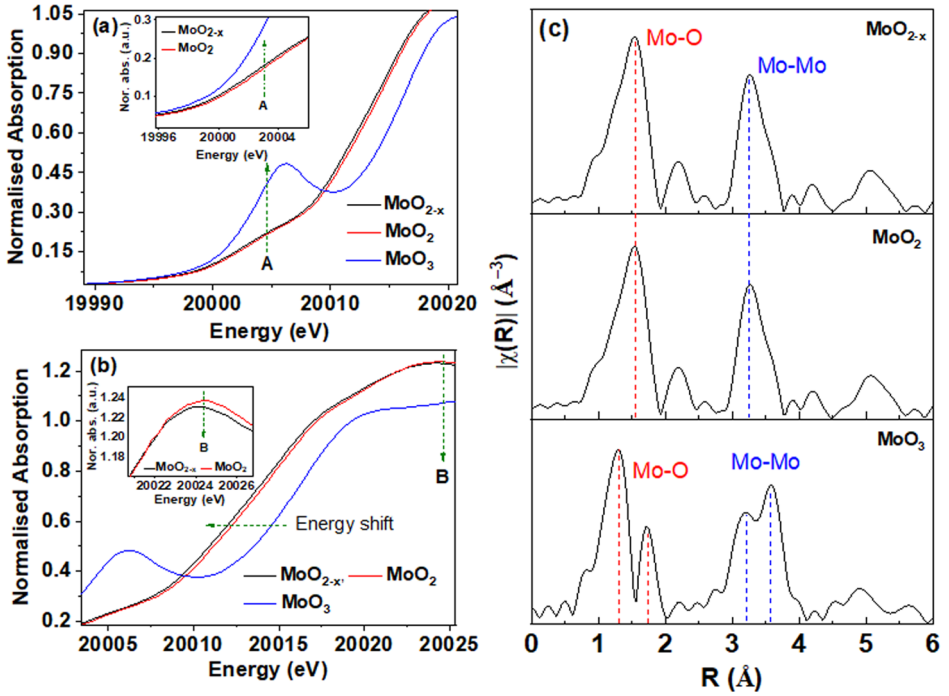

Figure 6. (a,b) XANES data of the as-synthesized and electrochemically activated MoO_2 along with data from the reference material. (c) FT-EXAFS of the as-synthesized and electrochemically activated MoO_2 along with that of the reference material.

for MoO_{2-x} is probably due to the reduction of surface-oxidized molybdenum ions in MoO_2 during electrochemical cycling.

XPS was monitored for the activated MoO_{2-x} and compared with the as-prepared one to understand any changes in the metal oxidation state during electrochemical activation. The Mo 3d spectra of the as-synthesized MoO_2 are deconvoluted into six peaks to represent the various oxidation states, such as Mo^{4+},Mo^{5+}, and Mo^{6+} ions (Figure 5a) that arise from surface oxidation. The peaks at 229.57 and 232.80 eV belong to $3d_{5/2}$ and $3d_{3/2}$ of Mo^{4+}, respectively, and the peaks due to the Mo^{5+} state appear at 231.20 ($3d_{5/2}$) and 234.63 eV ($3d_{3/2}$), whereas the peaks observed at 232.86 ($3d_{5/2}$) and 235.95 eV ($3d_{3/2}$) can be assigned to Mo^{6+}.[47]

The 3d spectra of activated MoO_{2-x} can also be deconvoluted into six peaks. The respective peaks assigned for the as-synthesized MoO_2 are seen shifted slightly to lower binding energies for the activated surface, indicating a reduction to intermediate lower oxidation states (Figure 5b). Accordingly, the peaks $3d_{5/2}$ and $3d_{3/2}$ seen at 228.90 and 232.14 eV, respectively,[48] are red-shifted by ~0.7 eV compared to those of Mo^{4+} of MoO_2 which can be denoted as Mo^{l+} ions (close to the Mo^{3+} state). The oxidation state of Mo^{l+} ions can be considered in between 3+ and 4+, indicating a reduced state of Mo^{4+}.[49] Similarly, 230.48 ($3d_{5/2}$) and 233.75 eV ($3d_{3/2}$) can be assigned to Mo^{m+} in the reduced state of Mo^{5+}, and that of Mo^{6+} state is reduced to Mo^{n+} at 232.65 ($3d_{5/2}$) and 235.25 eV ($3d_{3/2}$). Both Mo^{m+} and Mo^{n+} peaks are slightly red-shifted compared to the original positions of Mo^{5+} and Mo^{6+} ions (Figure 5a,b), and hence, the oxidation states of these ions are slightly lower than those of Mo^{5+} and Mo^{6+} ions ($5 > m > 4$ in Mo^{m+} and $6 > n > 5$ in Mo^{n+}), and this has been further proved by X-ray absorption spectroscopy (XAS) study. The O 1s spectra of MoO_2 are deconvoluted into three peaks such as O1 (lattice oxygen), O2 (defective site oxygen), and O3 (hydroxyl/surface adsorbed oxygen species) at 530.10, 531.56, and 533.05 eV, respectively (Figure S4).[50,51] The activated MoO_{2-x} gives O1, O2, O3, O4, and O5 peaks at 529.84, 532.06, 533.08, 533.76, and 535.62 eV, respectively. The additional O4 and O5 peaks arise from the Nafion binder used during electrochemical studies (O4—oxygen belongs to the sulfonate group of Nafion, and O5—oxygen in the ether

https://doi.org/10.1021/acsaem.3c00320
ACS Appl. Energy Mater. 2023, 6, 5342−5351

functional group of Nafion) (Figure S4).[52] The enhancement of the O2 peak relative to the O1 peak indicates the generation of defects in MoO_2 after electrochemical activation.[50] The various percentages of O1, O2, and O3 species in MoO_2 and MoO_{2-x} are shown in Table S1.

In order to glean further information about the development of MoO_{2-x} active sites and their local environment during activation, X-ray absorption spectroscopy (XAS) studies of the as-synthesized and electrochemically activated samples are performed. The X-ray absorption near-edge spectroscopy (XANES) of the as-synthesized MoO_2 gives the pre-edge around 20004.67 eV, and these features arise from 1s(Mo) → 4d(Mo) + 2p(O) electronic transition (Figure 6a). While this transition is forbidden for the regular MoO_6 octahedron (O_h), it becomes allowed for Mo systems with a distorted octahedron.[53] The amplitude of pre-edge depends on the degree of MoO_6 O_h distortion, 4d(Mo)/2p(O) orbital mixing, tetrahedral coordination, and coordinatively unsaturated distorted octahedral Mo sites,[53] and in summary, the variation in Mo K pre-edge can be related to MoO_6 distortion with lowering of the coordination environment. The white line peaks of the as-synthesized MoO_2 are observed at 20024.45 eV, and they are seen slightly shifted to a lower energy of 20023.93 eV in the electrochemically activated MoO_{2-x} arising from dipole-allowed 1s(Mo) → 5p(Mo) transition (Figure 6b inset). In the molybdenum compounds, the white line represents O_h geometrical features, and any changes are related to the distortion of the O_h geometry.[54] The MoO_2 pre-edge intensity (A in Figure 6a) slightly improves after electrochemical activation (Figure 6a inset). Furthermore, it represents the local environment/geometry of the catalyst distortion toward T_d/lower coordination with enhancement in HER activity. The oxidation state analysis by absorption edge reveals that after activation, the absorption edge moves toward lower energy than MoO_2 with a lowering of the white line intensity B (Figure 6b). The enhancement of pre-edge (A) and reduction in white line intensity (B) reveal that the active sites for HER get developed via O_h to T_d/lower geometrical transition in addition to the reduction in oxidation states of Mo (Figure 6a,b).

The Fourier transformed extended X-ray absorption fine structure spectra (FT-EXAFS) of MoO_2 before and after activation are given along with the pattern acquired from standard MoO_3 (Figure 6c). The spectra of the activated MoO_{2-x} show a pattern similar to that of MoO_2, rather than MoO_3, implying that the local environment of the activated catalyst closely resembles that of the as-synthesized MoO_2 (Figure 6c). However, a closer inspection of the FT-EXAFS of synthesized and activated MoO_2 catalysts given in Figure 7 reveals a slight reduction in the Mo−O and Mo−Mo coordination shell indicating the geometrical transition (O_h → T_d/lower) associated with a slight decrease of the coordination number of Mo−O and Mo−Mo shells. We have fitted the first-shell FT-EXAFS data of the as-synthesized and electrochemically activated MoO_2 (Figure S5). The initial average local coordination number of Mo−O gradually changes from 5.42 to 5.26 with the lowering of its oxidation state (Table S2 and Figure S5) and supports the surface defect formation in the active state of the catalyst for HER. This is reflected in the HER current density enhancement and lowering of the Tafel slope after 8000 potential cycles, as shown in Figure 1c. The altering of the Tafel slope reveals a change in the rate-determining step of HER, as explained below.

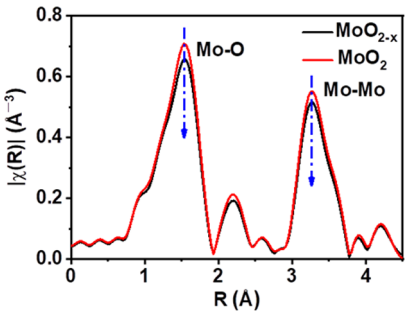

Figure 7. FT-EXAFS of the as-synthesized and electrochemically activated MoO_2.

Generally, the hydrogen evolution reaction proceeds through the following three steps,[55]

1. Volmer step,

$$H^+ + e^- \rightarrow H_{ads} \qquad b = 120 \quad mV/dec$$

The adsorption of the hydrogen ion by the Volmer step is followed by hydrogen gas evolution by the Heyrovsky or Tafel step. In the Heyrovsky step, the H^+ ions interact with H_{ads} species by transferring an electron from the electrode surface. In the Tafel step, the two adsorbed hydrogen ions interact and generate H_2. Both possible steps are given below with their Tafel slope values,[56]

2. Heyrovsky step,

$$H^+ + H_{ads} + e^- \rightarrow H_2 \quad b = 40 \quad mV/dec$$

3. Tafel step,

$$2H_{ads} \rightarrow H_2 \quad b = 30 \quad mV/dec$$

The as-synthesized MoO_2 gives a Tafel slope value of 127 mV/dec, close to 120 mV/dec, indicating that the Volmer step is the slow step with poor hydrogen adsorption. The activated MoO_{2-x} shows a Tafel slope value of 72 mV/dec, much lower than that of pristine MoO_2. The obtained Tafel slope value vividly indicates that HER on the MoO_{2-x} catalyst surface follows the Volmer−Heyrovsky reaction mechanism, with Heyrovsky being the rate-determining step, which is consistent with the earlier studies.[57,58] DFT study has further validated the HER mechanism on these catalyst surfaces. In order to assess consequent changes on electrochemical surface area (ECSA) during MoO_2 activation, ECSA values are estimated before and after electrochemical activation (Figure S6). The synthesized MoO_2 gives an ECSA of 37.42 cm^2, which greatly improves to 58.57 cm^2 after electrochemical activation and supports the development of active sites for hydrogen evolution. A comparison table of HER activity of the reported MoO_2-based systems is given in Table S3.

In order to rationalize the enhanced HER activity of the activated MoO_2 (MoO_{2-x}) over a bare MoO_2 catalyst surface, we have performed a first-principles-based density functional theory (DFT) study using the VASP simulation package[36] for both MoO_2 and MoO_{2-x} systems and evaluated the thermodynamic and kinetic parameters related to hydrogen evolution reaction on the catalyst surfaces. As revealed from HRTEM and XRD analysis, the surface-exposed plane of MoO_2 (110) is considered to be the active plane for electrochemical HER.[28,59] Moreover, electrochemically acti-

https://doi.org/10.1021/acsaem.3c00320
ACS Appl. Energy Mater. 2023, 6, 5342−5351

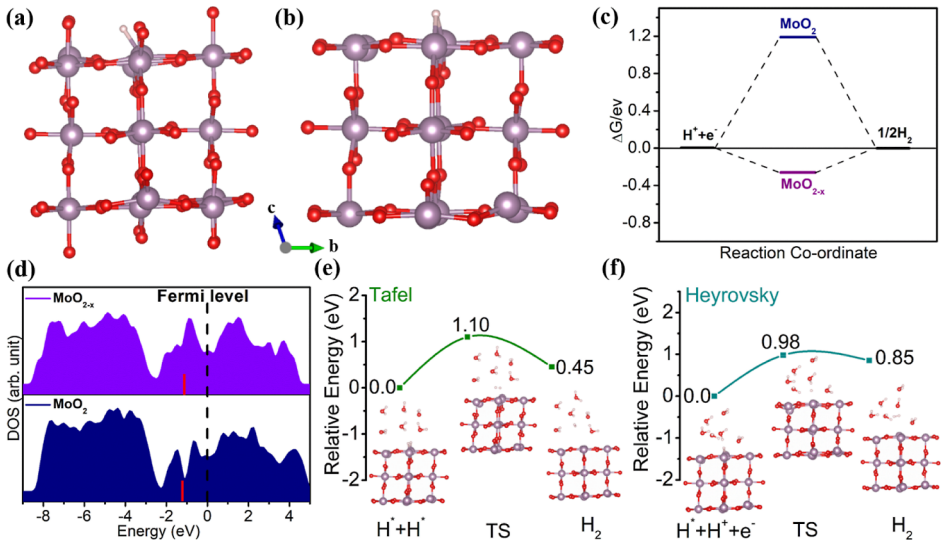

Figure 8. Optimized structures of H*-adsorbed (a) MoO_2 (110), (b) MoO_{2-x} (110) surfaces, (c) free energy diagram for H* adsorption on different MoO_x (110) surfaces for HER, (d) comparison between DOS plots of MoO_2 and MoO_{2-x} (110) surfaces (the positions of d-band centers (E_d) are indicated by the thick red bars), energy activation barriers for (e) Tafel, and (f) Heyrovsky step of HER on the MoO_{2-x} (110) surface.

vated MoO_2 is experimentally proven to be the oxide-deficient MoO_2 (MoO_{2-x}) surface through XPS and XAS analysis. The (110) surface of monoclinic MoO_2 consists of the surface-exposed terminal as well as bridging oxygen atoms, while on that of MoO_{2-x}, these surface-exposed terminal oxygen atoms are absent with Mo−O active centers exposed (Figure S7a,b). Here we have considered MoO_{2-x} (x = 0.37) based on the Mo−O local average coordination number of ∼5.26. More importantly, the active hexacoordinated Mo center exhibits octahedral geometry in pristine MoO_2, while the active Mo center in activated MoO_{2-x} is coordinatively unsaturated with distorted octahedral geometry. This finding corroborates well with the XAS analysis. Interestingly, this difference in the coordination environment of surface-exposed active Mo sites is expected to play a crucial role in HER.

The free energy diagram of H* adsorption on the catalyst surface is considered to be the key physical quantity to evaluate the HER activity of a catalyst.[41,60] The calculated change of Gibbs free energy for the most stable adsorption of hydrogen (ΔG_{H^*}) on various MoO_x surfaces is 1.19 and −0.26 eV, respectively, for bare MoO_2 and MoO_{2-x} catalysts (Figure 8a−c). The less stable hydrogen adsorption sites with corresponding ΔG_{H^*} values are shown in Figure S8. However, the adsorption of H* on a bare MoO_2(110) surface is thermodynamically unfavorable with a positive ΔG_{H^*} (1.19 eV). In contrast, a stronger and thermodynamically favorable H* adsorption is observed for the MoO_{2-x} (110) surface with ΔG_{H^*} = −0.26 eV. This difference in adsorption behavior can be attributed to the exposure of the active Mo center. On the bare MoO_2 (110) surface, due to the presence of terminal and bridging oxygen centers, H* adsorption is substantially hindered on the octahedral Mo center, leading to unfavorable adsorption. Instead, H* adsorption on the MoO_{2-x} (110) surface is highly facile and favorable due to surface-exposed and active, coordinatively unsaturated distorted octahedral Mo centers. According to the Sabatier principle, the most active catalytic site will have moderate hydrogen adsorption energy, with ΔG_{H^*} being close to zero.[61] Hence, MoO_{2-x} (110) is a better HER surface than bare MoO_2 (110).

The strong bonding interaction of H with the MoO_{2-x} (110) surface is well understood using the density of states (DOS) analysis. As evident from the DOS plot of H*-MoO_{2-x} (Figure S9a), the generation of the H 1s state is in the vicinity of −4.5, −6.5, and −7.8 eV (asterisk marks indicate a contribution from H 1s). Moreover, the projected density of states (PDOSs) analysis overwhelmingly exhibits the bonding interaction between H 1s and Mo s, p, and d-orbitals. However, even though there is a contribution from the Mo 5s orbital, the Mo 5d orbital mainly contributes to the Mo−H bond on MoO_x (110) surfaces (Figure S9b). The relatively stronger H* adsorption and hence better HER activity of the MoO_{2-x} (110) surface can be further justified by analyzing the positions of d-band centers (DBCs) of the catalysts.[62,63] As shown in Figure 8d, the DBC for the MoO_{2-x} (110) surface is −1.12 eV, while that for the MoO_2 (110) surface is −1.25 eV, indicating optimal H* adsorption and enhanced HER activity on the MoO_{2-x} (110) surface.

Besides thermodynamics, kinetics also plays a crucial role in catalysis.[41,64] To rationalize the detailed HER mechanism, we have calculated the activation barriers for two plausible pathways: Volmer−Tafel and Volmer−Heyrovsky (Figures 8 and S10 and Table S4). As depicted in Figure S10, the activation barrier for the H* adsorption step (i.e., Volmer step) is 5.18 eV which is higher compared to the evolution step (i.e., Tafel and Heyrovsky step) on the bare MoO_2 (110) surface, indicating that Volmer is the rate-determining step (r.d.s.) on this surface. Besides, the bare MoO_2 (110) surface also exhibits very high activation barriers of 4.10 and 4.85 eV, respectively, for the Tafel and Heyrovsky process, suggesting slower HER kinetics. On the other hand, substantially reduced activation barriers (0.90, 1.10, and 0.98 eV) are observed for Volmer, Tafel, and Heyrovsky steps on the MoO_{2-x} (110) surface, indicating much faster HER kinetics in this case. As evident from energy activation barriers, the Heyrovsky step is more favorable over the Tafel on the MoO_{2-x} (110) catalyst surface due to its lower activation barrier. Hence, from the kinetic study, it can be concluded that the MoO_{2-x} (110) surface follows the Volmer−Heyrovsky HER mechanism, with Heyrovsky being the r.d.s. This mechanistic study corroborates

https://doi.org/10.1021/acsaem.3c00320
ACS Appl. Energy Mater. 2023, 6, 5342−5351

with the experimentally determined reaction mechanism based on the Tafel slope value. Hence, based on thermodynamic and kinetic parameters, it can be concluded that MoO_{2-x} (110) will exhibit improved HER performance compared to the bare MoO_2 (110) surface, which is indeed observed experimentally.

The electrochemical impedance spectra of synthesized and activated MoO_2 are carried out at an applied potential of −0.55 V vs RHE (Figure 9). The impedance data are fitted with the equivalent circuit shown in Figure S11, and the obtained parameters are given in Table S5. R_s is solution resistance, R1 and CPE1 are resistance and constant phase element (represents capacitance) for hydrogen adsorption, respectively, and R2 and CPE2 represent charge-transfer resistance and capacitance for hydrogen evolution reaction, respectively (Table S5).[65,66] The lower charge-transfer resistance for MoO_{2-x} (76.4 Ω) compared to synthesized MoO_2 (148.4 Ω) supports improved HER activity with in-situ-generated active sites.

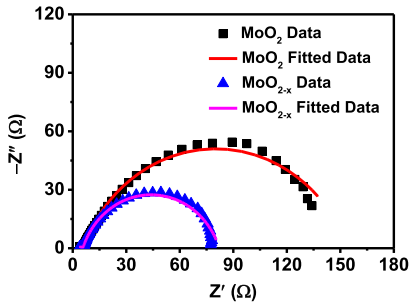

Figure 9. Impedance spectra of the as-synthesized and electrochemically activated MoO_2 at −0.55 V vs RHE (without *iR* correction).

CONCLUSIONS

The hydrogen evolution activity of poorly active as-synthesized MoO_2 is enhanced through in situ electrochemical activation. The gradual development of active sites and concurrent increment in HER activity are obtained by potential cycling. The X-ray absorption study reveals that the active sites start to develop by lowering the Mo−O coordination environment from octahedral (O_h) to coordinatively unsaturated distorted octahedral with a reduction of the oxidation state and coordination number as compared to synthesized MoO_2. The overpotential of electrochemically activated MoO_{2-x} is lowered by 0.2 V at 1 mA/cm^2 compared to MoO_2 with a drastic reduction of the Tafel slope from 127 to 72 mV/dec. The theoretical study reveals that the lowering of hydrogen adsorption free energy, ΔG_{H^*} close to zero, on the in-situ-generated active sites with surface oxygen defects significantly enhances HER activity. The energy activation barrier analysis for various elementary steps of hydrogen evolution reaction unveils that the generated active sites accelerate the reaction rate by altering the rate-determining step from Volmer to Heyrovsky.

ASSOCIATED CONTENT

Supporting Information

The Supporting Information is available free of charge at https://pubs.acs.org/doi/10.1021/acsaem.3c00320.

LSV curves without iR correction, LSV curve of bare FTO, FESEM images, XPS O 1s spectra, percentages of various species from XPS, EXAFS fitting details, ECSA calculation, HER activity comparison of MoO_2 based systems, optimized structures, DOS plots, activation energy barrier diagrams from DFT calculations, equivalent circuit model and extracted parameters from impedance data fitting (PDF)

AUTHOR INFORMATION

Corresponding Author

Neena S. John − *Centre for Nano and Soft Matter Sciences (CeNS), Bengaluru 562162, India;* orcid.org/0000-0001-6179-2150; Email: jsneena@cens.res.in

Authors

Chandraraj Alex − *Centre for Nano and Soft Matter Sciences (CeNS), Bengaluru 562162, India;* orcid.org/0000-0002-5620-2248

Rajkumar Jana − *School of Chemical Sciences, Indian Association for the Cultivation of Science (IACS), Kolkata 700032, India*

Vivek Ramakrishnan − *Centre for Nano and Soft Matter Sciences (CeNS), Bengaluru 562162, India;* Present Address: Department of Chemistry, Sree Sankara College, Affiliated to Mahatma Gandhi University, Kalady, Ernakulam, Kerala 683574, India; orcid.org/0000-0002-0283-5525

Muhammed Safeer Naduvil Kovilakath − *Centre for Nano and Soft Matter Sciences (CeNS), Bengaluru 562162, India; Manipal Academy of Higher Education, Manipal 576104, India*

Ayan Datta − *School of Chemical Sciences, Indian Association for the Cultivation of Science (IACS), Kolkata 700032, India;* orcid.org/0000-0001-6723-087X

Akhil Tayal − *Deutsches Elektronen-Synchrotron DESY, Hamburg 22607, Germany;* orcid.org/0000-0001-8152-4209

Complete contact information is available at: https://pubs.acs.org/10.1021/acsaem.3c00320

Notes

The authors declare no competing financial interest.

ACKNOWLEDGMENTS

DST, India, is acknowledged for funding provided within the framework of the India@DESY program. DESY (Hamburg, Germany), a member of the Helmholtz Association HGF, is acknowledged for the provision of experimental facilities. Parts of this research were carried out at PETRA III beamline P64, and the authors would like to thank Dr. Wolfgang A. Caliebe for beamline set-up. The beamtime was allocated for proposal I-20210655. The authors are thankful to Prof. G.U. Kulkarni for his support and encouragement. The authors C.A. and M.S.N.K. acknowledge the CeNS fellowship for financial assistance. The authors also thank the Central Research Facilities at CeNS, Bengaluru. The authors acknowledge Dr. Ashutosh K. Singh and Dr. Rajashekhar Pujar for the vacuum annealing facility. The authors also thank CeNSE, IISC for XPS measurements. R.J. thanks IACS and DST for the research fellowship, and A.D. thanks TRC-DST and SERB grant no. CRG/2020/000301 for partial funding.

REFERENCES

(1) Lin, Z.; Xiao, B.; Wang, Z.; Tao, W.; Shen, S.; Huang, L.; Zhang, J.; Meng, F.; Zhang, Q.; Gu, L.; Zhong, W. Planar-coordination $PdSe_2$ nanosheets as highly active electrocatalyst for hydrogen evolution reaction. *Adv. Funct. Mater.* **2021**, *31*, 2102321.

(2) Wang, Z.; Shen, S.; Lin, Z.; Tao, W.; Zhang, Q.; Meng, F.; Gu, L.; Zhong, W. Regulating the local spin state and band structure in Ni_3S_2 nanosheet for improved oxygen evolution activity. *Adv. Funct. Mater.* **2022**, *32*, 2112832.

(3) Zhang, L.; Wang, Z.; Zhang, J.; Lin, Z.; Zhang, Q.; Zhong, W.; Wu, G. High activity and stability in Ni_2P/(Co,Ni)OOH heterointerface with a multiple-hierarchy structure for alkaline hydrogen evolution reaction. *Nano Res.* **2023**, DOI: 10.1007/s12274-022-5322-2.

(4) Anantharaj, S.; Ede, S. R.; Sakthikumar, K.; Karthick, K.; Mishra, S.; Kundu, S. Recent trends and perspectives in electrochemical water splitting with an emphasis on sulfide, selenide, and phosphide catalysts of Fe, Co, and Ni: a review. *ACS Catal.* **2016**, *6*, 8069−8097.

(5) Alex, C.; Bhat, S. A.; John, N. S.; Yelamaggad, C. V. Highly Efficient and Sustained Electrochemical Hydrogen Evolution by Embedded Pd-Nanoparticles on a Coordination Polymer—Reduced Graphene Oxide Composite. *ACS Appl. Energy Mater.* **2019**, *2*, 8098−8106.

(6) Yan, Y.; Xia, B. Y.; Zhao, B.; Wang, X. A review on noble-metal-free bifunctional heterogeneous catalysts for overall electrochemical water splitting. *J. Mater. Chem. A* **2016**, *4*, 17587−17603.

(7) Browne, M. P.; Sofer, Z.; Pumera, M. Layered and two dimensional metal oxides for electrochemical energy conversion. *Energy Environ. Sci.* **2019**, *12*, 41−58.

(8) Zhu, J.; Hu, L.; Zhao, P.; Lee, L. Y. S.; Wong, K. Y. Recent advances in electrocatalytic hydrogen evolution using nanoparticles. *Chem. Rev.* **2019**, *120*, 851−918.

(9) Zhao, G.; Rui, K.; Dou, S. X.; Sun, W. Heterostructures for electrochemical hydrogen evolution reaction: a review. *Adv. Funct. Mater.* **2018**, *28*, 1803291.

(10) Zeng, M.; Li, Y. Recent advances in heterogeneous electrocatalysts for the hydrogen evolution reaction. *J. Mater. Chem. A* **2015**, *3*, 14942−14962.

(11) Zhao, H.; Li, Z.; Dai, X.; Cui, M.; Nie, F.; Zhang, X.; Ren, Z.; Yang, Z.; Gan, Y.; Yin, X.; et al. Heterostructured CoP/MoO_2 on Mo foil as high-efficiency electrocatalysts for the hydrogen evolution reaction in both acidic and alkaline media. *J. Mater. Chem. A* **2020**, *8*, 6732−6739.

(12) Chen, Z.; Duan, X.; Wei, W.; Wang, S.; Ni, B. J. Recent advances in transition metal-based electrocatalysts for alkaline hydrogen evolution. *J. Mater. Chem. A* **2019**, *7*, 14971−15005.

(13) Zhao, G.; Rui, K.; Dou, S. X.; Sun, W. Heterostructures for electrochemical hydrogen evolution reaction: a review. *Adv. Funct. Mater.* **2018**, *28*, 1803291.

(14) Liu, X.; Guo, Y.; Wang, P.; Wu, Q.; Zhang, Q.; Rozhkova, E. A.; Wang, Z.; Liu, Y.; Zheng, Z.; Dai, Y.; et al. Synthesis of Synergistic Nitrogen-Doped $NiMoO_4$/Ni_3N Heterostructure for Implementation of an Efficient Alkaline Electrocatalytic Hydrogen Evolution Reaction. *ACS Appl. Energy Mater.* **2020**, *3*, 2440−2449.

(15) Wang, J.; Mao, S.; Liu, Z.; Wei, Z.; Wang, H.; Chen, Y.; Wang, Y. Dominating role of Ni0 on the interface of Ni/NiO for enhanced hydrogen evolution reaction. *ACS Appl. Mater. Interfaces* **2017**, *9*, 7139−7147.

(16) Liu, X.; Dong, C.; Dong, W.; Wang, X.; Yuan, X.; Huang, F. Co nanoparticles embedded in a 3D CoO matrix for electrocatalytic hydrogen evolution. *RSC Adv.* **2016**, *6*, 38515−38520.

(17) Zhang, T.; Wu, M. Y.; Yan, D. Y.; Mao, J.; Liu, H.; Hu, W. B.; Du, X. W.; Ling, T.; Qiao, S. Z. Engineering oxygen vacancy on NiO nanorod arrays for alkaline hydrogen evolution. *Nano Energy* **2018**, *43*, 103−109.

(18) Li, Z.; Niu, W.; Zhou, L.; Yang, Y. Phosphorus and aluminum codoped porous NiO nanosheets as highly efficient electrocatalysts for overall water splitting. *ACS Energy Lett.* **2018**, *3*, 892−898.

(19) Ibupoto, Z. H.; Tahira, A.; Tang, P.; Liu, X.; Morante, J. R.; Fahlman, M.; Arbiol, J.; Vagin, M.; Vomiero, A. MoS_x@NiO composite nanostructures: an advanced nonprecious catalyst for hydrogen evolution reaction in alkaline media. *Adv. Funct. Mater.* **2019**, *29*, 1807562.

(20) Fang, L.; Jiang, Z.; Xu, H.; Liu, L.; guan, Y.; Gu, X.; Wang, Y. Crystal-plane engineering of $NiCo_2O_4$ electrocatalysts towards efficient overall water splitting. *J. Catal.* **2018**, *357*, 238−246.

(21) Guo, C.; Liu, X.; Gao, L.; Ma, X.; Zhao, M.; Zhou, J.; Kuang, X.; Deng, W.; Sun, X.; Wei, Q. Oxygen defect engineering in cobalt iron oxide nanosheets for promoted overall water splitting. *J. Mater. Chem. A* **2019**, *7*, 21704−21710.

(22) Luo, Z.; Miao, R.; Huan, T. D.; Mosa, I. M.; Poyraz, A. S.; Zhong, W.; Cloud, J. E.; Kriz, D. A.; Thanneeru, S.; He, J.; Zhang, Y.; et al. Mesoporous MoO_{3-x} material as an efficient electrocatalyst for hydrogen evolution reactions. *Adv. Energy Mater.* **2016**, *6*, 1600528.

(23) Datta, R. S.; Haque, F.; Mohiuddin, M.; Carey, B. J.; Syed, N.; Zavabeti, A.; Zhang, B.; Khan, H.; Berean, K. J.; Ou, J. Z.; Mahmood, N.; et al. Highly active two dimensional α-MoO_{3-x} for the electrocatalytic hydrogen evolution reaction. *J. Mater. Chem. A* **2017**, *5*, 24223−24231.

(24) Kaiser, F.; Schmidt, M.; Grin, Y.; Veremchuk, I. Molybdenum Oxides MoO_x: Spark-Plasma Synthesis and Thermoelectric Properties at Elevated Temperature. *Chem. Mater.* **2020**, *32*, 2025−2035.

(25) Xie, Q.; Zheng, X.; Wu, D.; Chen, X.; Shi, J.; Han, X.; Zhang, X.; Peng, G.; Gao, Y.; Huang, H. High electrical conductivity of individual epitaxially grown MoO_2 nanorods. *Appl. Phys. Lett.* **2017**, *111*, 093505.

(26) Jin, Y.; Shen, P. K. Nanoflower-like metallic conductive MoO_2 as a high-performance non-precious metal electrocatalyst for the hydrogen evolution reaction. *J. Mater. Chem. A* **2015**, *3*, 20080−20085.

(27) Ramakrishnan, V.; Alex, C.; Nair, A. N.; John, N. S. Designing metallic MoO_2 nanostructures on rigid substrates for electrochemical water activation. *Chem.—Eur. J.* **2018**, *24*, 18003−18011.

(28) Liu, X.; Ni, K.; Niu, C.; Guo, R.; Xi, W.; Wang, Z.; Meng, J.; Li, J.; Zhu, Y.; Wu, P.; Li, Q.; et al. Upraising the O 2p orbital by integrating Ni with MoO_2 for accelerating hydrogen evolution kinetics. *ACS Catal.* **2019**, *9*, 2275−2285.

(29) Zeng, H.; Chen, S.; Jin, Y. Q.; Li, J.; Song, J.; Le, Z.; Liang, G.; Zhang, H.; Xie, F.; Chen, J.; Jin, Y.; et al. Electron density modulation of metallic MoO_2 by Ni doping to produce excellent hydrogen evolution and oxidation activities in acid. *ACS Energy Lett.* **2020**, *5*, 1908−1915.

(30) Zhang, B.; Xue, Y.; Jiang, A.; Xue, Z.; Li, Z.; Hao, J. Ionic liquid as reaction medium for synthesis of hierarchically structured one-dimensional MoO_2 for efficient hydrogen evolution. *ACS Appl. Mater. Interfaces* **2017**, *9*, 7217−7223.

(31) Wang, B.; Zhang, Z.; Zhang, S.; Cao, Y.; Su, Y.; Liu, S.; Tang, W.; Yu, J.; Ou, Y.; Xie, S.; Li, J.; et al. Surface excited MoO_2 to master full water splitting. *Electrochim. Acta* **2020**, *359*, 136929.

(32) Wu, J. Q.; Zhao, J. W.; Li, G. R. Highly dispersed MoO_2 nanoparticles confined in N-doped porous carbon nanosheets for efficient hydrogen evolution in alkaline media. *Energy Fuels* **2020**, *34*, 9050−9057.

(33) Lin, S. H.; Kuo, J. L. Activating and tuning basal planes of MoO_2, MoS_2, and $MoSe_2$ for hydrogen evolution reaction. *Phys. Chem. Chem. Phys.* **2015**, *17*, 29305−29310.

(34) Caliebe, W. A.; Murzin, V.; Kalinko, A.; Görlitz, M. High-flux XAFS-beamline P64 at PETRA III. *AIP Conf. Proc.* **2019**, *2054*, 060031.

(35) Ravel, B.; Newville, M. ATHENA, ARTEMIS, HEPHAESTUS: data analysis for X-ray absorption spectroscopy using IFEFFIT. *J. Synchrotron Radiat.* **2005**, *12*, 537−541.

(36) Kresse, G.; Hafner, J. Ab initio molecular dynamics for liquid metals. *Phys. Rev. B: Condens. Matter Mater. Phys.* **1993**, *47*, 558−561.

(37) Perdew, J. P.; Burke, K.; Ernzerhof, M. Generalized gradient approximation made simple. *Phys. Rev. Lett.* **1996**, *77*, 3865−3868.

(38) Wang, F.; Pang, Z.; Lin, L.; Fang, S.; Dai, Y.; Han, S. Origin of magnetism in undoped MoO_2 studied by first-principles calculations. *Phys. Rev. B: Condens. Matter Mater. Phys.* **2010**, *81*, 134407.
(39) Grimme, S. Semiempirical GGA-type density functional constructed with a long-range dispersion correction. *J. Comput. Chem.* **2006**, *27*, 1787−1799.
(40) Cheng, X.; Li, Y.; Zheng, L.; Yan, Y.; Zhang, Y.; Chen, G.; Sun, S.; Zhang, J. Highly active, stable oxidized platinum clusters as electrocatalysts for the hydrogen evolution reaction. *Energy Environ. Sci.* **2017**, *10*, 2450−2458.
(41) Jana, R.; Chowdhury, C.; Malik, S.; Datta, A. Pt/Co_3O_4 Surpasses Benchmark Pt/C: An Approach Toward Next Generation Hydrogen Evolution Electrocatalyst. *ACS Appl. Energy Mater.* **2019**, *2*, 5613−5621.
(42) Borgschulte, A.; Sambalova, O.; Delmelle, R.; Jenatsch, S.; Hany, R.; Nüesch, F. Hydrogen reduction of molybdenum oxide at room temperature. *Sci. Rep.* **2017**, *7*, 40761.
(43) Duan, L.; Li, X. Lithiated Mo_4O_{11} to improve excellent cycle stability of MoO_2 nanoparticles for lithium-ion battery. *Synth. Met.* **2021**, *272*, 116672.
(44) Dieterle, M.; Mestl, G. Raman spectroscopy of molybdenum oxides Part II. Resonance Raman spectroscopic characterization of the molybdenum oxides Mo_4O_{11} and MoO_2. *Phys. Chem. Chem. Phys.* **2002**, *4*, 822−826.
(45) Wu, H.; Zhou, X.; Li, J.; Li, X.; Li, B.; Fei, W.; Zhou, J.; Yin, J.; Guo, W. Ultrathin molybdenum dioxide nanosheets as uniform and reusable surface-enhanced Raman spectroscopy substrates with high sensitivity. *Small* **2018**, *14*, 1802276.
(46) Camacho-López, M. A.; Escobar-Alarcón, L.; Picquart, M.; Arroyo, R.; Córdoba, G.; Haro-Poniatowski, E. Micro-Raman study of the m-MoO_2 to α-MoO_3 transformation induced by cw-laser irradiation. *Opt. Mater.* **2011**, *33*, 480−484.
(47) Borgschulte, A.; Sambalova, O.; Delmelle, R.; Jenatsch, S.; Hany, R.; Nüesch, F. Hydrogen reduction of molybdenum oxide at room temperature. *Sci. Rep.* **2017**, *7*, 40761−40769.
(48) Marin-Flores, O.; Scudiero, L.; Ha, S. X-ray diffraction and photoelectron spectroscopy studies of MoO_2 as catalyst for the partial oxidation of isooctane. *Surf. Sci.* **2009**, *603*, 2327−2332.
(49) Marin-Flores, O.; Scudiero, L.; Ha, S. X-ray diffraction and photoelectron spectroscopy studies of MoO_2 as catalyst for the partial oxidation of isooctane. *Surf. Sci.* **2009**, *603*, 2327−2332.
(50) Cao, Y.; Liang, P.; Dong, Q.; Wang, D.; Zhang, D.; Tang, L.; Wang, L.; Jin, S.; Ni, D.; Yu, Z. Facile reduction method synthesis of defective MoO_{2-x} nanospheres used for SERS detection with high chemical enhancement. *Anal. Chem.* **2019**, *91*, 8683−8690.
(51) Guha, P.; Mohanty, B.; Thapa, R.; Kadam, R. M.; Satyam, P. V.; Jena, B. K. Defect-engineered MoO_2 nanostructures as an efficient electrocatalyst for oxygen evolution reaction. *ACS Appl. Energy Mater.* **2020**, *3*, 5208−5218.
(52) Friedman, A. K.; Shi, W.; Losovyj, Y.; Siedle, A. R.; Baker, L. A. Mapping microscale chemical heterogeneity in Nafion membranes with X-ray photoelectron spectroscopy. *J. Electrochem. Soc.* **2018**, *165*, H733−H741.
(53) Jonane, I.; Cintins, A.; Kalinko, A.; Chernikov, R.; Kuzmin, A. X-ray absorption near edge spectroscopy of thermochromic phase transition in $CuMoO_4$. *Low Temp. Phys.* **2018**, *44*, 434−437.
(54) Brookes, C.; Wells, P. P.; Dimitratos, N.; Jones, W.; Gibson, E. K.; Morgan, D. J.; Cibin, G.; Nicklin, C.; Mora-Fonz, D.; Scanlon, D. O.; Catlow, C. R. A.; et al. The nature of the molybdenum surface in iron molybdate. The active phase in selective methanol oxidation. *J. Phys. Chem. C* **2014**, *118*, 26155−26161.
(55) Jayabal, S.; Saranya, G.; Wu, J.; Liu, Y.; Geng, D.; Meng, X. Understanding the high-electrocatalytic performance of two-dimensional MoS_2 nanosheets and their composite materials. *J. Mater. Chem. A* **2017**, *5*, 24540−24563.
(56) Jin, H.; Guo, C.; Liu, X.; Liu, J.; Vasileff, A.; Jiao, Y.; Zheng, Y.; Qiao, S. Z. Emerging two-dimensional nanomaterials for electrocatalysis. *Chem. Rev.* **2018**, *118*, 6337−6408.
(57) Prats, H.; Chan, K. The determination of the HOR/HER reaction mechanism from experimental kinetic data. *Phys. Chem. Chem. Phys.* **2021**, *23*, 27150−27158.
(58) Bao, F.; Kemppainen, E.; Dorbandt, I.; Bors, R.; Xi, F.; Schlatmann, R.; Krol, R.; Calnan, S. Understanding the Hydrogen Evolution Reaction Kinetics of Electrodeposited Nickel-Molybdenum in Acidic, Near-Neutral, and Alkaline Conditions. *ChemElectroChem* **2021**, *8*, 195−208.
(59) Ji, J.; Aleisa, R. M.; Duan, H.; Zhang, J.; Yin, Y.; Xing, M. Metallic active sites on MoO_2 (110) surface to catalyze advanced oxidation processes for efficient pollutant removal. *iScience* **2020**, *23*, 100861.
(60) Nørskov, J. K.; Bligaard, T.; Logadottir, A.; Kitchin, J. R.; Chen, J. G.; Pandelov, S.; Stimming, U. Trends in the exchange current for hydrogen evolution. *J. Electrochem. Soc.* **2005**, *152*, J23.
(61) Bligaard, T.; Nørskov, J. K.; Dahl, S.; Matthiesen, J.; Christensen, C. H.; Sehested, J. The Brønsted−Evans−Polanyi relation and the volcano curve in heterogeneous catalysis. *J. Catal.* **2004**, *224*, 206−217.
(62) Mavrikakis, M.; Hammer, B.; Nørskov, J. K. Effect of strain on the reactivity of metal surfaces. *Phys. Rev. Lett.* **1998**, *81*, 2819−2822.
(63) Hammer, B.; Norskov, J. K. Why gold is the noblest of all the metals. *Nature* **1995**, *376*, 238−240.
(64) Jana, R.; Datta, A.; Malik, S. Tuning intermediate adsorption in structurally ordered substituted $PdCu_3$ intermetallic nanoparticles for enhanced ethanol oxidation reaction. *Chem. Commun.* **2021**, *57*, 4508−4511.
(65) Abbas, S. A.; Iqbal, M. I.; Kim, S. H.; Jung, K. D. Catalytic activity of urchin-like Ni nanoparticles prepared by solvothermal method for hydrogen evolution reaction in alkaline solution. *Electrochim. Acta* **2017**, *227*, 382−390.
(66) Bai, L.; Harrington, D. A.; Conway, B. E. Behaviour of overpotential—deposited species in Faradaic reactions—II. ac Impedance measurements on H_2 evolution kinetics at activated and unactivated Pt cathodes. *Electrochim. Acta* **1987**, *32*, 1713−1731.

https://doi.org/10.1021/acsaem.3c00320
ACS Appl. Energy Mater. 2023, 6, 5342−5351